Systematic study of electronic structure and band alignment of monolayer transition metal dichalcogenides in Van der Waals heterostructures

2017 2D Mater. 4 015026

(http://iopscience.iop.org/2053-1583/4/1/015026)

2D Materials

RECEIVED
28 June 2016

REVISED
2 November 2016

ACCEPTED FOR PUBLICATION
14 November 2016

PUBLISHED
30 November 2016

PAPER

Systematic study of electronic structure and band alignment of monolayer transition metal dichalcogenides in Van der Waals heterostructures

Chenxi Zhang[1,6], Cheng Gong[1,6], Yifan Nie[1], Kyung-Ah Min[2], Chaoping Liang[1], Young Jun Oh[1], Hengji Zhang[3], Weihua Wang[1,5], Suklyun Hong[2], Luigi Colombo[4], Robert M Wallace[1,3] and Kyeongjae Cho[1,3]

[1] Department of Materials Science and Engineering, The University of Texas at Dallas, Richardson, TX 75080, USA
[2] Department of Physics and Graphene Research Institute, Sejong University, Seoul 143-747, Korea
[3] Department of Physics, The University of Texas at Dallas, Richardson, TX 75080, USA
[4] Texas Instruments, Dallas, TX 75243, USA
[5] Department of Electronics and Tianjin Key Laboratory of Photo-Electronic Thin Film Device and Technology, Nankai University, Tianjin, 30071, China
[6] These authors equally contributed to this work.

E-mail: kjcho@utdallas.edu

Keywords: transition metal dichalcogenides (TMDs), band alignment, devices, heterostructure, electronic structure, density functional theory (DFT)

Supplementary material for this article is available online

Abstract

Two-dimensional transition metal dichalcogenides (TMDs) are promising low-dimensional materials which can produce diverse electronic properties and band alignment in van der Waals heterostructures. Systematic density functional theory (DFT) calculations are performed for 24 different TMD monolayers and their bilayer heterostacks. DFT calculations show that monolayer TMDs can behave as semiconducting, metallic or semimetallic depending on their structures; we also calculated the band alignment of the TMDs to predict their alignment in van der Waals heterostacks. We have applied the charge equilibration model (CEM) to obtain a quantitative formula predicting the highest occupied state of any type of bilayer TMD heterostacks (552 pairs for 24 TMDs). The CEM predicted values agree quite well with the selected DFT simulation results. The quantitative prediction of the band alignment in the TMD heterostructures can provide an insightful guidance to the development of TMD-based devices.

1. Introduction

Two-dimensional (2D) materials, arising from the isolation of graphene by Geim and Novoselov, have received extensive attention among the materials research communities because of their novel properties and rich low-dimensional physics [1]. The novel properties of two-dimensional (2D) materials have driven a rapid development of graphene-based nanoscale electronic devices and fundamental research of new physics [2]. The boom of research in 2D materials have stimulated a renewed interest in layered crystalline materials with unique electrical and optical properties [3].

Regarded as an outstanding representative, transition metal dichalcogenides (TMDs) ranging from metal, semi-metal to semiconductors have demonstrated their potential significance in the exploration of future nanoelectronic devices [4]. Their superior material properties such as direct band gap, atomic thickness and large degree of electrostatic control, enable a large number of applications in electronic (semiconductor [5–7], superconductor [8]), photonic (photoluminescence [9, 10], photo-sensor [11], solar energy harvesting [12]), thermal [13, 14], mechanical (solid lubricants), catalytic [15, 16] and emerging spintronic and valleytronic devices [17–19].

Considering the large number of metal dichalcogenides materials, systematic studies of the structural and electronic properties of the TMD family are necessary as a prerequisite of exploiting TMDs-based devices. In the 1980s, Grasso *et al* have reviewed the electronic properties of a series of bulk layered materials based on an augmented plane wave method [20].

Recently, substantial efforts have also been devoted to understanding the basic electronic properties of monolayer TMDs including electronic band gaps [21–23], work functions, and electron/hole effective masses [24–26]. which are required for diverse device applications. In addition, many state of the art simulation methods have been applied to monolayer TMDs to investigate their detailed band structures [21, 22, 27–32]. To understand the band structure of monolayer TMDs, the spin orbit coupling (SOC) effect needs to be considered because of the lack of inversion symmetry in monolayer TMDs [17, 33, 34]. Z Y Zhu *et al* showed that the spin–orbit interaction induces a splitting of ~0.15 eV at the topmost valence band in monolayer H-MoS_2. The SOC splitting is even larger for monolayer TMDs with heavy transition metal elements because the SOC strength increases rapidly with the increasing atomic number of constituent elements [35]. Although the primary characteristics can be described by DFT simulation with generalized gradient approximation of Perdew–Burke–Ernzerhof functionals (GGA-PBE), due to the existence of exciton binding energy, there is a ~1 eV difference between optical band gap and quasi-particle (QP) band gap. To accurately capture the features of the band structure, many-body perturbation *GW* theory was used to investigate both monolayer and bilayer TMDs which yielded band gap values in good agreement with experimental results [3, 28, 36–43].

More recently, in addition to monolayer TMDs-based devices, the focus of developing 2D vertical heterostructure (van der Waals stack of diverse 2D crystals) devices have been put into the study of p–n junction devices [44], photoluminescent devices [45–47], photovoltaic devices [48–50], photodetectors [51], light emitting diode (LED) [52]. Because of weak van der Waals interaction between TMDs layers and their atomic commensurability (i.e. compatible stacking of TMDs with different lattice constants), it is easy to reassemble them into large varieties of heterostructures. Due to the availability of versatile electrical properties of monolayer TMDs spanning from semiconductor to metal and superconductor, a broad range of material parameter space is opened up to design and obtain desired TMD heterostack properties for next-generation electronic devices [53, 54]. Nevertheless, applications of 2D crystals in heterostructure devices are intrinsically determined by the fundamental structural and electronic properties of constituent 2D materials, especially by their band alignment when the 2D van der Waals heterostack is formed. Recent modeling papers have provided useful database of universal band alignment of 2D transition metal oxides and chalcogenides with respect to the vacuum [23, 35, 36, 40]. This provides insightful guidance for experimentalists to optimize the electrical contacts [55, 56], and design heterogeneous junctions with dissimilar materials [57–59]. However, when the two 2D materials are stacked, the band alignment is not simply a superposition of bands of two components. Some additional effect such as interfacial charge polarization and redistribution occurs which cannot be well described by Mott-Schottky rule [60] or Anderson's rule [61] in conventional semiconducting heterostructures.

Moreover, it is extremely expensive and time consuming to experimentally test the electrical properties of a large number of 2D heterostacks to explore the desired band alignments. Therefore, to further understand such stacking effects at the van der Waals heterostructure interface, a systematic investigation on the band alignments of the TMDs heterostacks is necessary.

In this work, we firstly use density functional theory (DFT) calculations to examine the relative phase stability between trigonal prismatic structure (noted as H), octahedral structure (noted as T) and distorted octahedral structure (T′) in 24 types of 2D TMDs which are the combinations of group IV–VI transition metals and chalcogen species (S, Se, and Te). After determining the most stable phases of those TMDs, their band structures with SOC are calculated and the band alignments of monolayer TMDs are summarized with respect to the vacuum level. To more accurately describe the band alignment, the G_0W_0 method is also applied to some semiconducting TMDs. After establishing the reference band alignment information, we use the DFT method to study the band alignments in the heterostacks of two monolayer TMDs with similar lattice constants which can be classified into three categories: (1) semiconductor–metal stack, (2) semiconductor-semiconductor stack and (3) semiconductor–semimetal stack. Finally, by analyzing the band alignments of these heterostacks, we developed a formula to predict the band alignments of stacked varying TMDs using charge equilibration method (CEM).

2. Methodology

The calculations are performed using the Vienna *ab initio* simulation package [62]. The projector-augmented wave [63] pseudopotentials are adopted, and both local density approximation (LDA) [64] and generalized gradient approximation (GGA) of Perdew–Burke–Ernzerhof (PBE) [65] functionals are used to describe the exchange-correlation potential. We optimized structures of monolayer transition metals (group IV: Ti, Zr and Hf; group V: V, Nb, and Ta; and group VI: Mo and W) dichalcogenides (S, Se, and Te) using both GGA-PBE and LDA. For convenience, we define 'n-TMD' to represent different types of single layer TMDs in which n is the transition metal group number. A vacuum thickness of ~16 Å is set for monolayer TMDs to avoid periodic image interactions during atomic relaxation. With a cutoff energy of 400 eV, the ionic relaxation stops with the residual

force on each atom is less than 0.01 eV $Å^{-1}$ and the electronic optimization stops when total energy difference is smaller than 10^{-4} eV. The Monkhorst-Pack k-point sampling in Brillouin zone (BZ) is Γ-centered with 8 × 8 × 1 and 40 × 40 × 1 meshes in ionic and electronic optimization, respectively. We summarize the thermodynamic stability of various TMDs (the T structure, the H structure and in some instance distorted T structure noted as T′ structure) by comparing their total energy with reference to that of the T phase.

Considering van der Waals interactions in TMD bilayer heterostructures, we include the Grimme DFT-D3 correction with GGA-PBE functional for atomic relaxation [66]. Energetically more stable hexagonal AB stacking model is used for bilayer TMDs heterostructures [67].

To understand the details of the electronic structure of monolayer TMDs, band structure calculations with and without SOC are performed along high symmetry points in the BZ with GGA-PBE. The band gaps of semiconducting monolayer TMDs are summarized and analyzed.

With respect to the vacuum level, the universal band alignments of all the TMDs with energetically favorable phases are performed. The dipole correction is included along the direction perpendicular to the surface of TMDs [68].

The G_0W_0 calculations are also performed to get more accurate band alignments of some semiconducting monolayer TMDs, with a cutoff energy of 400 eV and 128 empty bands. In QP G_0W_0 calculations, Γ centered 12 × 12 × 1 Monkhorst-Pack k-point mesh is used for BZ integration. Since the band gap center (BGC) is reported to be insensitive to different exchange-correlation functionals [69], we employ the method proposed by Toroker *et al* to determine the band edge positions [70]. The corrected conduction band minimum (CBM) and valence band maximum (VBM) is given by

$$E_{\mathrm{CBM/VBM}} = E_{\mathrm{BGC}} \pm \frac{1}{2}E_{\mathrm{g}}^{\mathrm{QP}}, \qquad (1)$$

where E_{BGC} is the band gap center energy obtained by PBE functional and $E_{\mathrm{g}}^{\mathrm{QP}}$ is the quasiparticle band gap from the G_0W_0 calculation.

3. Results and discussions

3.1. Band alignment of monolayer TMDs

To determine the band alignment information of isolated monolayer TMDs, we firstly study the phase stability of various monolayer TMDs and then investigate their electronic structures. Due to the hugeness of detailed band structures of relevant monolayer TMDs, they are listed in the supporting information as a database. By using the band structure information database of various monolayer TMDs, we can easily extract their band gaps and absolute band positions with respect to vacuum. The results of CBM, VBM and band gap obtained by GGA-PBE and G_0W_0 method are tabulated in table 1. The band gaps obtained by including the SOC effect in this work are similar to or slightly smaller than the values reported previously [30]. This behavior is especially obvious in W-based H-monolayer TMDs due to a large SOC effect of ∼0.4 eV at the VBE which is consistent with previous works [3]. The work function results of some monolayer TMDs agree very well with reported values. Moreover, the calculated electron affinity ∼4.27 eV of monolayer MoS_2 agrees well with the experimentally reported electron affinity ∼4.0 eV in bulk MoS_2 crystals [71, 72].

To have a clear picture of band alignments of various monolayer TMDs, the VBM and CBM are plotted with green and orange columns in figure 1 respectively. The chart is divided into three parts in which the left part is the band alignment of semiconducting monolayer TMDs. The middle and right parts are metallic and semimetallic monolayer TMDs with only occupied states marked. The results are consistent with the most recent work on the two-dimensional metal–semiconductor junction [73].

As shown in figure 1, for the H-monolayer VI-TMDs, when the atomic indexes of chalcogen species increase from S to Te, the VBE undergoes a conspicuous energy increase, associated with a relatively smaller energy increase of the CBE, resulting in a decreasing energy gap. At the same time, the larger atomic radius and decreased reactivity induce weakened interaction between transition metal atoms and chalcogen atoms and correspondingly a larger lattice constant, thus resulting in a decrease in the band gaps. For the same chalcogen species, Mo is more reactive than W because of the intrinsic higher reactivity of 3d-electrons compared to 4d-electrons. Therefore, the overall energy levels of Mo-dichalcogenides are lower than that of W-dichalcogenides. The six outermost valence electrons of metal atoms are bonded to six chalcogen atoms through trigonal prismatic coordination. Therefore, the valence band can be fully saturated while the conduction band is not occupied, inducing the semiconducting nature of H-monolayer VI-TMDs.

In contrast to group VI TM atoms, group IV TM atoms have two less valence electrons. As a result, IV-TMDs are semiconducting with deeper bands with respect to VI-TMDs. It is consistent with the observation of higher work functions of IV-TMDs than those of VI-TMDs. The same semiconducting nature but distinctive positions of band edges of VI- and IV-TMDs indicate the potential combination of these two types of TMDs for TFET application. For example, electrons at the VBE of WSe_2 would be able to tunnel into the conduction band of ZrS_2 with ease. Another promising couple for a TFET device is WSe_2 with SnS_2 or $SnSe_2$, and for this reason the band alignments of SnS_2 and $SnSe_2$ are also shown in figures 1 and 2 [74].

Table 1. VBM (E_v), CBM (E_c) and band gaps (E_g) of different monolayer TMDs are listed. E_c can also be referenced as electron affinity (EA) which is the energy difference between CBM and vacuum level. 'D' and 'I' in the parenthesis of E_g (D/I) indicate 'direct' and 'indirect' band gaps. 'M' and 'SM' denote the metallic and semimetallic nature of monolayer TMDs respectively. The work functions (WF) of semiconducting monolayer TMDs are calculated by $-(E_c + E_v)/2$ and the work functions of semimetallic and metallic monolayer TMDs are calculated by the difference between VBM of DFT result to the vacuum level.

	DFT			G_0W_0					
TMDs	E_v (eV)	E_c (eV)	E_g (eV)	E_v (eV)	E_c (eV)	E_g (eV)	WF(eV)	Method	Reference
H-MoS_2	**−5.86**	**−4.27**	**1.59 (D)**	**−6.42**	**−3.71**	**2.71**	**5.07**	PBE	
			1.68 (D)	−6.28	−3.92	2.36	5.10	PBE	[37]
	−6.13	−4.55	1.58 (D)	−6.32	−3.84	2.48		LDA	[38]
H-$MoSe_2$	**−5.23**	**−3.88**	**1.32 (D)**	**−5.75**	**−3.38**	**2.37**	**4.57**	PBE	
			1.45 (D)	−5.62	−3.58	2.04	4.60	PBE	[37]
	−5.50	−4.18	1.32 (D)	−5.63	−3.46	2.18		LDA	[38]
H-$MoTe_2$	**−4.75**	**−3.78**	**0.94 (D)**	**−5.24**	**−3.35**	**1.89**	**4.29**	PBE	
			1.08 (D)	−5.12	−3.58	1.54	4.35	PBE	[37]
	−5.04	−4.11	0.93 (D)	−5.11	−3.40	1.71		LDA	[38]
H-WS_2	**−5.50**	**−3.93**	**1.54 (D)**	**−6.19**	**−3.28**	**2.91**	**4.73**	PBE	
			1.82 (D)	−6.11	−3.47	2.64	4.79	PBE	[37]
	−5.75	−4.24	1.51 (D)	−6.28	−3.85	2.43		LDA	[38]
H-WSe_2	**−4.86**	**−3.55**	**1.32 (D)**	**−5.49**	**−2.92**	**2.57**	**4.21**	PBE	
			1.55 (D)	−5.46	−3.20	2.26	4.33	PBE	[37]
	−5.13	−3.91	1.22 (D)	−5.61	−3.53	2.08		LDA	[38]
H-WTe_2	**−4.44**	**−3.69**	**0.74 (D)**	**−4.20**	**−2.55**	**1.93**	**4.06**	PBE	
			1.07 (D)	−4.97	−3.35	1.62	4.16	PBE	[37]
T-ZrS_2	**−6.38**	**−5.30**	**1.08 (I)**	**−7.19**	**−4.49**	**2.70**	**5.84**	PBE	
			1.19 (I)	−7.14	−4.58	2.56	5.86	PBE	[37]
	−6.58	−5.55	1.03 (I)	−5.61	−3.53	2.88		LDA	[38]
T-$ZrSe_2$	**−5.44**	**−5.15**	**0.29 (I)**	**−6.19**	**−4.41**	**1.78**	**5.30**	PBE	
			0.50 (I)	−6.14	−4.60	1.54	5.37	PBE	[37]
	−5.66	−5.41	0.25 (I)	−6.53	−4.68	1.85		LDA	[38]
T-HfS_2	**−5.73**	**−5.71**	**1.23 (I)**	**−7.16**	**−4.27**	**2.89**	**5.71**	PBE	
			1.27 (I)	−6.98	−4.53	2.45	5.75	PBE	[37]
	−6.48	−5.42	1.06 (I)	−7.92	−4.63	2.98		LDA	[38]
T-$HfSe_2$	**−4.91**	**−5.37**	**0.45 (I)**	**−6.14**	**−4.19**	**1.95**	**5.17**	PBE	
			0.61 (I)	−5.95	−4.56	1.39	5.25	PBE	[37]
	−5.57	−5.26	0.30 (I)	−6.53	−4.58	1.96		LDA	[38]
T-SnS_2	**−7.05**	**−5.46**	**1.59 (I)**	**−7.77**	**−4.74**	**3.04**	**6.55**	PBE	
	−6.98	−5.58	1.40 (I)	−7.98	−4.91	3.07		LDA	[38]
T-$SnSe_2$	**−6.00**	**−5.22**	**0.78 (I)**	**−6.57**	**−4.74**	**1.84**	**5.79**	PBE	
	−6.19	−5.58	0.62 (I)	−6.96	5.05	1.91		LDA	[38]
H-VSe_2	**−5.51**	**−5.33**	**0.18(I)**	M	M	M	**5.42**	PBE	
H-VTe_2	−5.00	−4.83	0.17(I)	M	M	M	4.92	PBE	
H-VS_2	−5.92	SM	SM	M	M	M	5.92	PBE	
T-VS_2	−5.53	M	M	M	M	M	5.51	PBE	
T-VSe_2	−5.00	M	M	M	M	M	5.55	PBE	
T-VTe_2	−4.60	M	M	M	M	M	4.60	PBE	
H-NbS_2	−6.07	M	M	M	M	M	6.09	PBE	
T-NbS_2	−5.33	M	M	M	M	M	5.32	PBE	
H-$NbSe_2$	−5.54	M	M	M	M	M	5.52	PBE	
T-$NbSe_2$	−4.91	M	M	M	M	M	4.90	PBE	
H-$NbTe_2$	−5.02	M	M	M	M	M	5.06	PBE	
T-$NbTe_2$	−5.14	M	M	M	M	M	4.62	PBE	
H-TaS_2	−5.91	M	M	M	M	M	5.93	PBE	
T-TaS_2	−5.09	M	M	M	M	M	5.06	PBE	
H-$TaSe_2$	−5.38	M	M	M	M	M	5.40	PBE	
T-$TaSe_2$	−4.68	M	M	M	M	M	4.66	PBE	
H-$TaTe_2$	−4.82	M	M	M	M	M	4.90	PBE	
T-$TaTe_2$	−4.83	M	M	M	M	M	4.40	PBE	
T-TiS_2	−5.74	SM	SM	SM	SM	SM	5.72	PBE	
T-$TiSe_2$	−5.32	SM	SM	SM	SM	SM	5.32	PBE	
T-$TiTe_2$	−4.81	SM	SM	SM	SM	SM	4.86	PBE	
T-$ZrTe_2$	−4.81	SM	SM	SM	SM	SM	4.56	PBE	
T-$HfTe_2$	−4.70	SM	SM	SM	SM	SM	4.72	PBE	

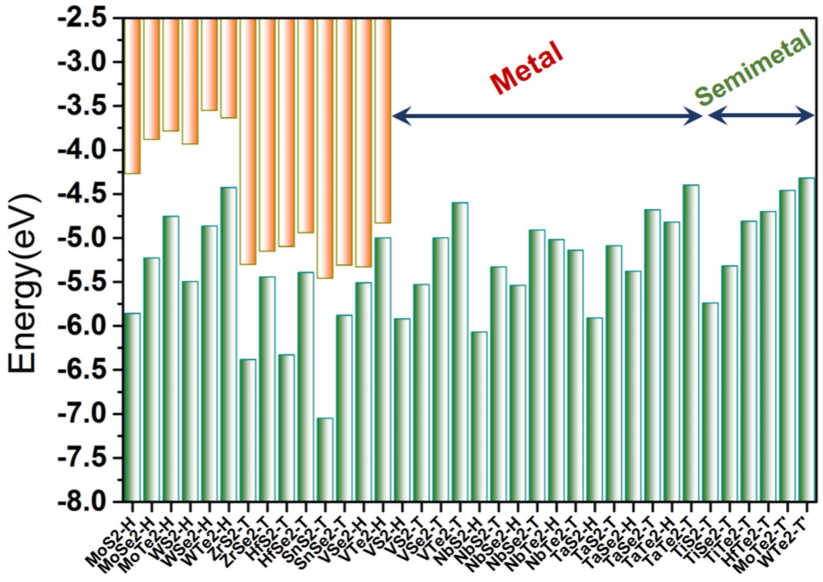

Figure 1. Band alignment of all the studied monolayer TMDs. CBM and VBM are indicated by the green and orange columns respectively. The vacuum level is set to 0 eV.

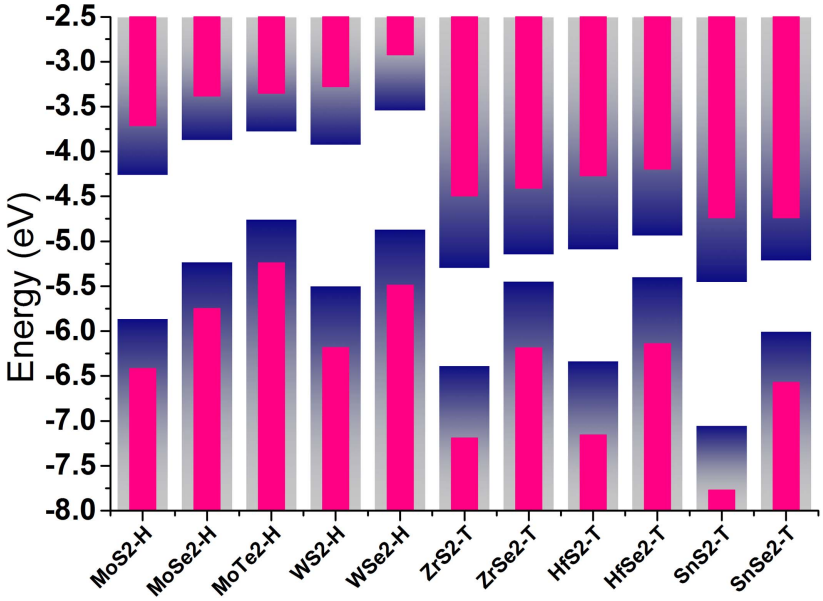

Figure 2. Position of band edges for stable semiconducting TMDs with respect to vacuum. The band edge of DFT-PBE data and G_0W_0 data are indicated by filled navy blue gradient column and pink solid column, respectively. The vacuum level is set to 0 eV.

Different from VI-TMDs and IV-TMDs, most H- and T- monolayer V-TMDs are metallic except for H-VSe_2 and H-VTe_2 have already been reported to be semiconducting or metallic [38, 75]. A half-occupied band is produced because of the lack of one valance electron in group V TM atoms compared to group VI transition metal atoms. Thus all V-TMDs become metallic with intermediate work functions between VI-TMDs and IV-TMDs. Such diverse electronic properties of 2D TMDs make this emerging family of low-dimensional materials promising for a broad range of applications.

To predict a more accurate band alignment, we applied the G_0W_0 method to correct the band gaps of the semiconducting monolayer TMDs. By aligning the center of the Fermi level of *GW* calculation and GGA-PBE calculation, VBE and CBE are estimated, respectively, by shifting equally half of the G_0W_0 band gap from the band center calculated by GGA-PBE. The corrected band edges and band gaps are listed in table 1. This kind of shifting was also reported by Liang *et al*, showing that the band gap of MoS_2 will have a shift of about 50% of the *GW* band gap from the center of Fermi level calculated by GGA-PBE [27]. It is found

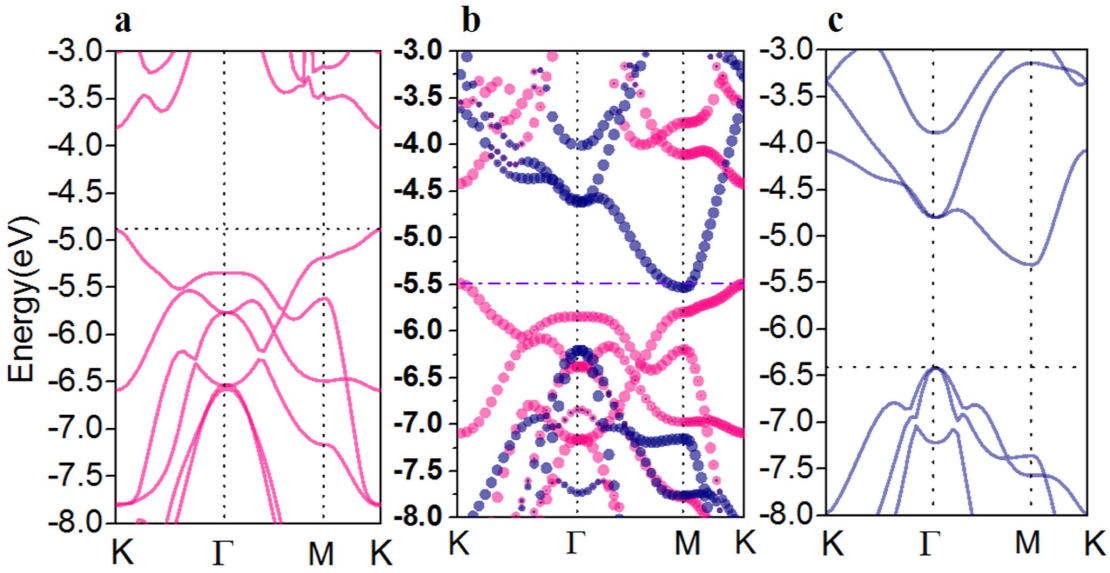

Figure 3. The band structure of isolated (a) monolayer H-$MoTe_2$ and (c) monolayer T-ZrS_2 are plotted with pink solid lines and navy solid lines respectively. The horizontal black dotted lines indicate Fermi level in the isolated monolayer H-$MoTe_2$ and T-ZrS_2. The projected band structure of H-$MoTe_2$ layer and T-ZrS_2 layer in H-$MoTe_2$–T-ZrS_2 bilayer heterostack are indicated by pink dotted lines and navy dotted lines respectively. The violet dash dotted line represent the Fermi level in the H-$MoTe_2$–T-ZrS_2 bilayer heterostack. The vacuum level is set to be zero.

that the band gaps agree with or are slightly larger than previously reported values [3, 21, 27, 28, 37, 38]. These differences may arise from the SOC effect and the difference in computational details including software package, pseudopotentials and detailed settings. The G_0W_0 corrected band edges of monolayer VI-TMDs agree with previously reported results except for a ~0.2 eV difference which may be due to the spin–orbit splitting [38]. Some band edge positions obtained from PBE and LDA methods are quite different, which results from the difference between PBE and LDA in describing the exchange correlation effect. The conduction and valence band offset of the WSe_2 and MoS_2 couple are also consistent with the experimental measurement showing the validity of our calculation [47]. Note that the work function of $HfSe_2$ (~5.2 eV) disagrees with recent experimental values (~3.8–4.4 eV) to some extent [76]. This is attributed to the utilization of a perfect crystalline sample in the DFT calculation, while in the real measurement, considerable amount of defects are contained in the samples which will lead to a different work function value. It is also worthy to note that the difference between the DFT band gap and *GW* band gap originates from the band gap renormalization by the reduced screening of Coulomb interaction [39]. As we have shown recently, the dielectric environment can provide strong screening of Coulomb interaction and reduce the *GW* band gap down to DFT band gap by removing the band gap renormalization [77]. Consequently, the band gaps of a monolayer TMD can have intermediate values between DFT and *GW* band gaps depending upon the dielectric environment of the heterostructures.

All of the band alignment information can facilitate the development of future heterostructure device development. For example, by using the alignment information, appropriate combination of monolayer metallic and semiconducting TMDs can be found to form a good metal–semiconductor contact thus reducing the contact resistance. As the band alignment is used to determine the interlayer band gap and electron transition behavior, it can be used to develop new 2D LED and photovoltaic devices [45–47]. However, such band alignment provides a rough guideline, and more quantitative band structure alignment in TMD heterostructure require further analysis.

3.2. Band alignment in TMD bilayer heterostructures

After getting the band alignment information of the building block monolayer TMDs, we can have a blueprint for designing diverse promising heterostructure devices. However, when two monolayer TMDs are stacked, the resultant band structure of the heterostacks is not a simple combination of two monolayer TMDs which is commonly described by Mott-Schottky or Anderson's rule [59, 60]. Some additional effects occur at the interfaces including charge transfer, charge redistribution and interfacial dipoles leading to the shift of the band alignment. These phenomena were experimentally observed in previous publications [78–80].

To understand the band alignment before and after the stacking of two monolayer TMDs, we choose a set of monolayer TMDs with negligible mismatch in their lattice constants to calculate the band structure of their heterostacks.

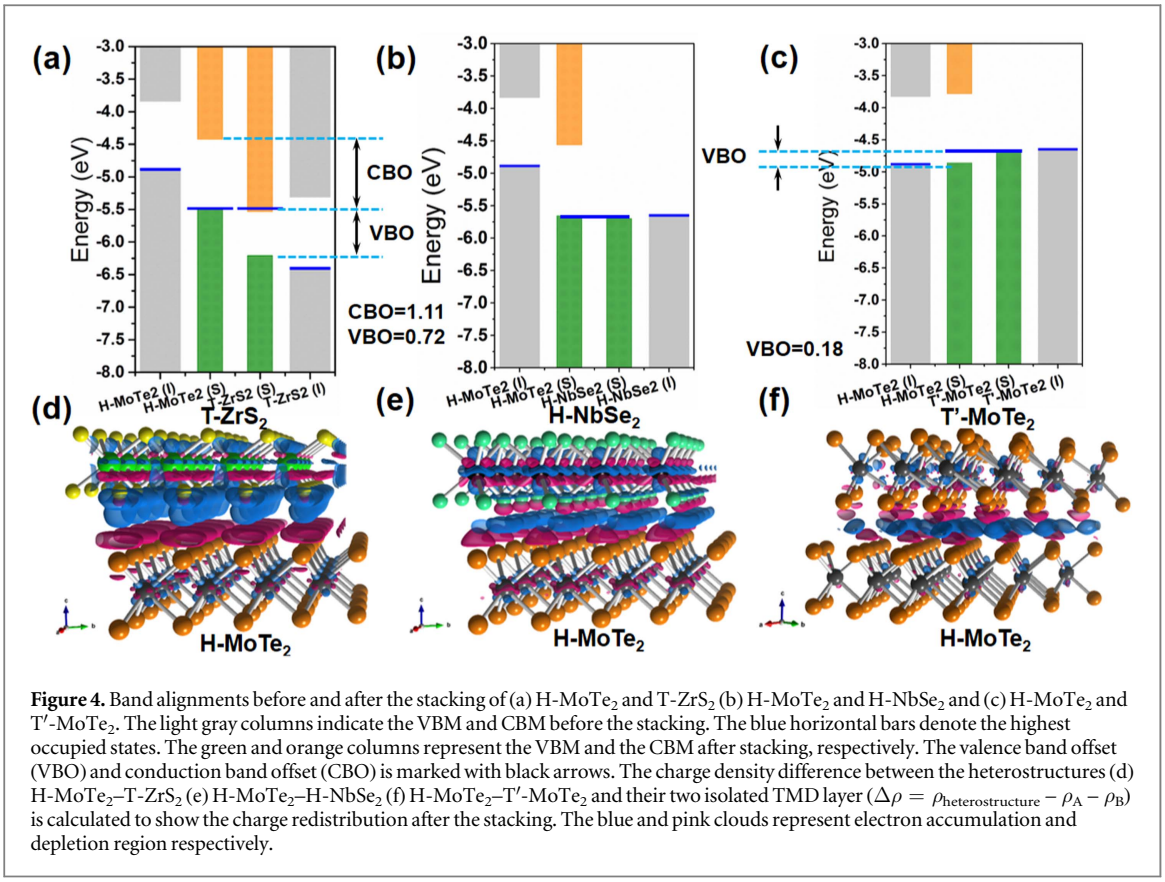

Figure 4. Band alignments before and after the stacking of (a) H-$MoTe_2$ and T-ZrS_2 (b) H-$MoTe_2$ and H-$NbSe_2$ and (c) H-$MoTe_2$ and T′-$MoTe_2$. The light gray columns indicate the VBM and CBM before the stacking. The blue horizontal bars denote the highest occupied states. The green and orange columns represent the VBM and the CBM after stacking, respectively. The valence band offset (VBO) and conduction band offset (CBO) is marked with black arrows. The charge density difference between the heterostructures (d) H-$MoTe_2$–T-ZrS_2 (e) H-$MoTe_2$–H-$NbSe_2$ (f) H-$MoTe_2$–T′-$MoTe_2$ and their two isolated TMD layer ($\Delta\rho = \rho_{\text{heterostructure}} - \rho_A - \rho_B$) is calculated to show the charge redistribution after the stacking. The blue and pink clouds represent electron accumulation and depletion region respectively.

The band structure of monolayer H-$MoTe_2$, monolayer T-ZrS_2 and their heterostacks are shown in figure 3. The valence band edge of isolated monolayer H-$MoTe_2$ is higher than the conduction band edge of isolated monolayer T-ZrS_2. As a result, when monolayer H-$MoTe_2$ is in contact with monolayer T-ZrS_2, the band structure of H-$MoTe_2$–T-ZrS_2 bilayer heterostack is not a simple superposition of their individual band structures; charge transfer is observed from the valence band of monolayer H-$MoTe_2$ to the conduction band of monolayer T-ZrS_2. This charge transfer can also be confirmed by the partially occupied valence band and conduction band around the Fermi level in the H-$MoTe_2$–T-ZrS_2 bilayer heterostack (see figure 3(b)). Comparing the band structure of monolayer H-$MoTe_2$ in figure 3(a) and the projected band structure of H-$MoTe_2$ in figure 3(b), we can find similar amount of lowering in the conduction band and the valence band which keeps the band gap almost the same. Note that in T-ZrS_2 the conduction band is shifted down and the valence is shifted up respectively. The inconsistency of the trend of band shifts between H-$MoTe_2$ and T-ZrS_2 can be regarded as a complex interfacial effect including dipole formation, charge redistribution, interlayer coupling etc.

By extracting the VBM, CBM and Fermi level from the band structure before and after stacking (like figure 3), we investigated the band alignment of H-$MoTe_2$–T-ZrS_2, H-$MoTe_2$–H-$NbSe_2$ and H-$MoTe_2$–T′-$MoTe_2$ bilayer heterostructures. These three couples represent three types of heterostacks including: semiconductor–semiconductor, semiconductor–metal and metal–semimetal. The band alignment variations of these three combinations before (light gray) and after (VBM-green column, CBM-orange column) stacking are shown in figures 4(a), (b) and (c) respectively.

First, in the H-$MoTe_2$–T-ZrS_2 stack (semiconductor-semiconductor stack), as the VBM of H-$MoTe_2$ is located at a higher energy than the CBM of T-ZrS_2, a charge transfer from H-$MoTe_2$ to T-ZrS_2 can be observed as shown in figure 4(d). The highest occupied state of the heterostack is aligned with the VBM of H-$MoTe_2$ after stacking. The charge transfer and interlayer coupling have been experimentally observed in many previous publications [78, 79, 81, 82]. Moreover, in the H-$MoTe_2$–T-ZrS_2 stack, the valence band offset (VBO) and the conduction band offset (CBO) between H-$MoTe_2$ layer and T-ZrS_2 layer is calculated to be 0.72 eV and 1.11 eV respectively. It is interesting to see that the band gap of H-$MoTe_2$ is almost unchanged before and after stacking while the band gap of T-ZrS_2 is slightly reduced due to the complex interlayer coupling and the interfacial charges.

Second, in the H-$MoTe_2$–H-$NbSe_2$ stack (semiconductor–metal stack), because the average energies of electrons in H-$MoTe_2$ is higher than that of H-$NbSe_2$, the charge transfer occurs from the VBM of H-$MoTe_2$ to H-$NbSe_2$ (shown in figure 4(e)). The

valence band of H-$MoTe_2$ is shifted down to be aligned with the VBM of the stack, while the VBM of H-$NbSe_2$ is just slightly lowered because the charge injection cannot change the Fermi level due to the existence of empty states around the highest occupied state of H-$NbSe_2$.

Third, in the H-$MoTe_2$–T′-$MoTe_2$-stack (semiconductor–semimetal stack), similar to the semiconductor–metal stack such as H-$MoTe_2$–H-$NbSe_2$ stack, the charge transfer from T′-$MoTe_2$ to H-$MoTe_2$ is almost negligible which can be confirmed by the tiny upshift of the VBM and CBM of H-$MoTe_2$ after stacking. This effect can be seen in figure 4(f), compared to figures 4(d) and (e), where more transferred charge is accumulated in the interface rather than in the charge accepting layer. Similar to metal, the shift of VBE positions in T′-$MoTe_2$ is very small because of its semimetallic nature. The reason for the small charge transfer is the small difference in chemical potential (in another word the Fermi level) between the H-$MoTe_2$ and T′-$MoTe_2$. The Schottky barrier between H-$MoTe_2$ and T′-$MoTe_2$ is 0.18 eV which is close to ohmic contact.

In addition to the heterostacks described above, we also investigated many other TMDs bilayer heterostacks described above. Their detailed band structures and alignments are shown in figures S10–S17, and the band offsets are listed in table S3. These data are critical for the design and development of heterostructure devices.

It is worthwhile to note that in the semiconductor–metal and semiconductor–semimetal stacks, the realignments reduce the Schottky barrier heights which greatly reduce the contact resistance and improve the electrical performance of TMDs heterostructure based field effect transistors (FETs). Theoretically it has been shown that the Schottky barrier can be tuned by choosing various metallic TMDs as contact electrodes. Due to the Van der Waals contact, 2D metal can have the advantages including facilitating carrier transport, weakened Fermi level pinning and reduced electron-hole recombination [73]. Experimentally, improved contact resistance is also observed in WSe_2–$NbSe_2$ FETs and the formation of ohmic homojunction in $MoTe_2$ [54, 83].

Although we have some understanding of band alignment variation in several Van der Waals heterostacks of TMDs from DFT calculations, considering large number of heterostructures, it still takes huge amount of time and resource to experimentally explore the band alignments of these heterostructures. Furthermore, direct DFT modeling of all possible TMD bilayer heterostacks also has practical challenges of lattice mismatch among different TMDs. Therefore, a conclusive formula predicting the band alignment of the heterostack based on the alignment of component monolayer TMDs is necessary for the heterostructure design.

Table 2. ϕ_A and ϕ_B is the highest occupied state of isolated layer A and layer B. Layer A and layer B indicates the bottom and upper TMD layer in the heterostructure. For example layer A represents H-$MoTe_2$ layer and layer B represents T-ZrS_2 layer in the H-$MoTe_2$–T-ZrS_2 heterostructure. ϕ_{DFT} is the highest occupied state of the heterostructure consisting of layer A and layer B calculated by DFT simulation and $\phi_{formula}$ is the highest occupied state of the heterostructure obtained by our formula. ϕ_{DFT} and $\phi_{formula}$ show good agreement between each other.

Heterostructure	ϕ_A	ϕ_B	ϕ_{DFT}	$\phi_{Formula}$
H-$MoTe_2$–T-ZrS_2	4.89	6.41	5.49	5.52
H-$MoTe_2$–T-$ZrSe_2$	4.89	5.58	5.26	5.18
H-WSe_2–H-NbS_2	5.11	6.08	6.12	6.08
H-$MoTe_2$–H-$NbSe_2$	4.89	5.55	5.52	5.55
H-WSe_2–H-$NbSe_2$	5.11	5.55	5.41	5.55
H-$MoTe_2$–T-$NbSe_2$	4.89	4.91	4.96	4.91
H-$MoSe_2$–H-$NbSe_2$	5.33	5.55	5.52	5.55
H-$MoSe_2$–H-NbS_2	5.33	6.08	6.07	6.08
H-$MoTe_2$–T′-$MoTe_2$	4.89	4.49	4.68	4.49

By referring to the CEM used in double-wall nanotubes, we developed a formula to predict the highest occupied state of the heterostack from the highest occupied state of its building block monolayer TMDs. The DFT results and the predicted results are tabuated in table 2 which agree very well with the largest difference of ∼0.2 eV. By analyzing the applicability of the formula, we find that it has better agreement for the heterostructures with a higher amount of charge transfer. On the other hand, there is acceptable agreement in the H-$MoTe_2$–T′-$MoTe_2$ heterostack in which charge transfer is least obvious (see figure 4(f)). The reason for such difference in applicability of this formula may come from additional processes occurring at the interface including charge redistribution and interlayer coupling.

4. Conclusions

We have performed comprehensive DFT calculations to investigate phase stability, electronic structures, band alignments, work functions of 2D transition metal (group IV: Ti, Zr and Hf; group V: V, Nb, and Ta; and group VI: Mo and W) dichalcogenides (S, Se, and Te). A clear trend of the preferential intralayer coordination is found to be determined by the electronic configuration of transition metal atoms. The TMDs studied here cover direct- and indirect-gap semiconductors, metals and semi-metals. In particular, the universal band alignment information of the studied TMD family can provide experimentalists with valuable guidance for designing electrical contacts, TFETs and photovoltaic devices based on heterogeneous stacking of TMD films. A conclusive formula based on CEM is developed to predict the band alignments of a large number of TMD bilayer heterostructures. This quick and easy method to estimate the band alignment of the heterostructure by the band positions of arbitrary TMD components will

provide helpful guidance for the development of numerous promising TMD heterostructure nanoelectronic devices.

Acknowledgments

This work was supported by the Center for Low Energy Systems Technology (LEAST), one of six centers supported by the STARnet phase of the Focus Center Research Program (FCRP), a Semiconductor Research Corporation program sponsored by MARCO and DARPA. This work is partially supported by Nano Material Technology Development Program (2012M3A7B4049888) through the National Research Foundation of Korea (NRF) funded by the Ministry of Science, ICT and Future Planning, and Priority Research Center Program (2010-0020207) through NRF funded by the Ministry of Education. CZ would like to thank Professor Massimo Fischetti at the University of Texas at Dallas for providing computational resources and Professor William G H Vendenberghe for valuable discussions.

References

[1] Geim A K and Novoselov K S 2007 *Nat. Mater.* **6** 183
[2] Ferrari A C *et al* 2015 *Nanoscale* **7** 4598
[3] Yazyev O V and Kis A 2015 *Mater. Today* **18** 20
[4] Wang Q H, Kalantar-Zadeh K, Kis A, Coleman J N and Strano M S 2012 *Nat. Nanotechnol.* **7** 699
[5] Mak K F, Lee C, Hone J, Shan J and Heinz T F 2010 *Phys. Rev. Lett.* **105** 136805
[6] Cheng L, Qin X, Lucero A T, Azcatl A, Huang J, Wallace R M, Cho K and Kim J 2014 *ACS Appl. Mater. Interfaces* **6** 11834
[7] Radisavljevic B, Radenovic A, Brivio J, Giacometti V and Kis A 2011 *Nat. Nanotechnol.* **6** 147
[8] Sipos B, Kusmartseva A F, Akrap A, Berger H, Forró L and Tutiš E 2008 *Nat. Mater.* **7** 960
[9] Splendiani A, Sun L, Zhang Y, Li T, Kim J, Chim C-Y, Galli G and Wang F 2010 *Nano Lett.* **10** 1271
[10] Eda G, Yamaguchi H, Voiry D, Fujita T, Chen M and Chhowalla M 2011 *Nano Lett.* **11** 5111
[11] Yin Z, Li H, Li H, Jiang L, Shi Y, Sun Y, Lu G, Zhang Q, Chen X and Zhang H 2011 *ACS Nano* **6** 74
[12] Li L, Wang H, Fang X, Zhai T, Bando Y and Golberg D 2011 *Energy Environ. Sci.* **4** 2586
[13] Chiritescu C, Cahill D G, Nguyen N, Johnson D, Bodapati A, Keblinski P and Zschack P 2007 *Science* **315** 351
[14] Muratore C, Varshney V, Gengler J, Hu J, Bultman J, Smith T, Shamberger P, Qiu B, Ruan X and Roy A 2013 *Appl. Phys. Lett.* **102** 081604
[15] Karunadasa H I, Montalvo E, Sun Y, Majda M, Long J R and Chang C J 2012 *Science* **335** 698
[16] Voiry D, Salehi M, Silva R, Fujita T, Chen M, Asefa T, Shenoy V B, Eda G and Chhowalla M 2013 *Nano Lett.* **13** 6222
[17] Mak K F, He K, Shan J and Heinz T F 2012 *Nat. Nanotechnol.* **7** 494
[18] Zeng H, Dai J, Yao W, Xiao D and Cui X 2012 *Nat. Nanotechnol.* **7** 490
[19] Cao T *et al* 2012 *Nat. Commun.* **3** 887
[20] Grasso V 1986 *Electronic Structure and Electronic Transitions in Layered Materials* vol 7 (Berlin: Springer) (doi:10.1007/978-94-009-4542-5)
[21] Kang J, Tongay S, Zhou J, Li J and Wu J 2013 *Appl. Phys. Lett.* **102** 012111
[22] Kang J, Tongay S, Li J and Wu J 2013 *J. Appl. Phys.* **113** 143703
[23] Gong C, Zhang H, Wang W, Colombo L, Wallace R M and Cho K 2013 *Appl. Phys. Lett.* **103** 053513
[24] Chang J, Register L F and Banerjee S K 2013 *Appl. Phys. Lett.* **103** 223509
[25] Liu L, Kumar S B, Ouyang Y and Guo J 2011 *IEEE Trans. Electron Devices* **58** 3042
[26] Ilatikhameneh H, Tan Y, Novakovic B, Klimeck G, Rahman R and Appenzeller J 2015 *IEEE J. Explor. Solid-State Comput. Devices Circuits* **1** 12
[27] Liang Y, Huang S, Soklaski R and Yang L 2013 *Appl. Phys. Lett.* **103** 042106
[28] Shi H, Pan H, Zhang Y-W and Yakobson B I 2013 *Phys. Rev.* B **87** 155304
[29] Peelaers H and Van de Walle C G 2012 *Phys. Rev.* B **86** 241401
[30] Yun W S, Han S, Hong S C, Kim I G and Lee J 2012 *Phys. Rev.* B **85** 033305
[31] Han S, Kwon H, Kim S K, Ryu S, Yun W S, Kim D, Hwang J, Kang J-S, Baik J and Shin H 2011 *Phys. Rev.* B **84** 045409
[32] Cheiwchanchamnangij T and Lambrecht W R 2012 *Phys. Rev.* B **85** 205302
[33] Roldán R, López-Sancho M P, Guinea F, Cappelluti E, Silva-Guillén J and Ordejón P 2014 *2D Mater.* **1** 034003
[34] Cappelluti E, Roldán R, Silva-Guillén J, Ordejón P and Guinea F 2013 *Phys. Rev.* B **88** 075409
[35] Zhu Z Y, Cheng Y C and Schwingenschlögl U 2011 *Phys. Rev.* B **84** 153402
[36] Komsa H-P and Krasheninnikov A V 2013 *Phys. Rev.* B **88** 085318
[37] Zhuang H L and Hennig R G 2013 *J. Phys. Chem.* C **117** 20440
[38] Rasmussen F A and Thygesen K S 2015 *J. Phys. Chem.* C **119** 13169
[39] Ugeda M M *et al* 2014 *Nat. Mater.* **13** 1091
[40] Debbichi L, Eriksson O and Lebègue S 2014 *Phys. Rev.* B **89** 205311
[41] He J, Hummer K and Franchini C 2014 *Phys. Rev.* B **89** 075409
[42] Jiang H 2012 *J. Phys. Chem.* C **116** 7664
[43] Roldán R, Silva-Guillén J A, López-Sancho M P, Guinea F, Cappelluti E and Ordejón P 2014 *Ann. Phys.* **526** 347
[44] Lee C-H, Lee G-H, van Der Zande A M, Chen W, Li Y, Han M, Cui X, Arefe G, Nuckolls C and Heinz T F 2014 *Nat. Nanotechnol.* **9** 676
[45] Rivera P, Schaibley J R, Jones A M, Ross J S, Wu S, Aivazian G, Klement P, Seyler K, Clark G and Ghimire N J 2015 *Nat. Commun.* **6** 6242
[46] Gong Y, Lin J, Wang X, Shi G, Lei S, Lin Z, Zou X, Ye G, Vajtai R and Yakobson B I 2014 *Nat. Mater.* **13** 1135
[47] Chiu M-H, Zhang C, Shiu H-W, Chuu C-P, Chen C-H, Chang C-Y S, Chen C-H, Chou M-Y, Shih C-K and Li L-J 2015 *Nat. Commun.* **6** 7666
[48] Furchi M M, Pospischil A, Libisch F, Burgdörfer J and Mueller T 2014 *Nano Lett.* **14** 4785
[49] Wi S, Kim H, Chen M, Nam H, Guo L J, Meyhofer E and Liang X 2014 *ACS Nano* **8** 5270
[50] Shanmugam M, Jacobs-Gedrim R, Song E S and Yu B 2014 *Nanoscale* **6** 12682
[51] Britnell L *et al* 2013 *Science* **340** 1311
[52] Withers F *et al* 2015 *Nat. Mater.* **14** 301
[53] Geim A K and Grigorieva I V 2013 *Nature* **499** 419
[54] Terrones H, López-Urías F and Terrones M 2013 *Sci. Rep.* **3** 1549
[55] Cho S *et al* 2015 *Science* **349** 625
[56] Kappera R, Voiry D, Yalcin S E, Branch B, Gupta G, Mohite A D and Chhowalla M 2014 *Nat. Mater.* **13** 1128
[57] Li M-Y, Chen C-H, Shi Y and Li L-J 2015 *Mater. Today* **19** 322
[58] Wang H, Liu F, Fu W, Fang Z, Zhou W and Liu Z 2014 *Nanoscale* **6** 12250
[59] Nie Y, Hong S, Wallace R M and Cho K 2016 *Nano Lett.* **16** 2090
[60] Bardeen J 1974 *Phys. Rev.* **71** 717
[61] Anderson R L 1960 *IBM J. Res. Dev.* **4** 283
[62] Kresse G and Furthmüller J 1996 *Comput. Mater. Sci.* **6** 15
[63] Blöchl P E 1994 *Phys. Rev.* B **50** 17953
[64] Ceperley D M and Alder B 1980 *Phys. Rev. Lett.* **45** 566

[65] Perdew J P, Burke K and Ernzerhof M 1996 *Phys. Rev. Lett.* **77** 3865
[66] Grimme S, Antony J, Ehrlich S and Krieg H 2010 *J. Chem. Phys.* **132** 154104
[67] Liu K, Zhang L, Cao T, Jin C, Qiu D, Zhou Q, Zettl A, Yang P, Louie S G and Wang F 2014 *Nat. Commun.* **5** 4966
[68] Neugebauer J and Scheffler M 1992 *Phys. Rev.* B **46** 16067
[69] Zhuang H L and Hennig R G 2013 *Chem. Mater.* **25** 3232
[70] Toroker M C, Kanan D K, Alidoust N, Isseroff L Y, Liao P and Carter E A 2011 *Phys. Chem. Chem. Phys.* **13** 16644
[71] Hughes H P and Starnberg H 2001 *Electron Spectroscopies Applied to Low-Dimensional Structures* vol 24 (Berlin: Springer) (doi:10.1007/0-306-47126-4)
[72] Li M O, Esseni D, Snider G, Jena D and Xing H G 2014 *J. Appl. Phys.* **115** 074508
[73] Liu Y, Stradins P and Wei S-H 2016 *Sci. Adv.* **2** e1600069
[74] Roy T, Tosun M, Hettick M, Ahn G H, Hu C and Javey A 2016 *Appl. Phys. Lett.* **108** 083111
[75] Li F, Tu K and Chen Z 2014 *J. Phys. Chem.* C **118** 21264
[76] Yue R, Barton A T, Zhu H, Azcatl A, Pena L F, Wang J, Peng X, Lu N, Cheng L and Addou R 2014 *ACS Nano* **9** 474
[77] Ryou J, Kim Y-S, Santosh K C and Cho K 2016 *Sci. Rep.* **6** 29184
[78] Zhang J *et al* 2016 *Adv. Mater.* **28** 1950
[79] Ceballos F, Bellus M Z, Chiu H-Y and Zhao H 2015 *Nanoscale* **7** 17523
[80] Tongay S *et al* 2014 *Nano Lett.* **14** 3185
[81] He J, Kumar N, Bellus M Z, Chiu H-Y, He D, Wang Y and Zhao H 2014 *Nat. Commun.* **5** 5622
[82] Palummo M, Bernardi M and Grossman J C 2015 *Nano Lett.* **15** 2794
[83] Kim A R *et al* 2016 *Nano Lett.* **16** 1890